A Cryogenic, High-field Trap for Large Positron Plasmas and Cold Beams

J. R. Danielson, P. Schmidt, J.P. Sullivan[1], and C. M. Surko

Department of Physics, University of California, San Diego, La Jolla, CA 92093-0319
1. Photon Factory, High Energy Accelerator Research Organization, Japan

A new Penning-Malmberg trap using a 5 tesla magnetic field and a cryogenic electrode structure (T~10K) has been constructed with the goal of producing large ($N \geq 10^{10}$), high-density positron plasmas and cold positron beams ($\Delta\varepsilon \sim 1$ meV). With background pressures $\leq 10^{-11}$ torr and rotating electric fields to counteract plasma expansion due to background asymmetries, this trap is designed to be a nearly ideal reservoir of positrons with very long confinement and annihilation times. This paper describes recent experiments using electron plasmas to optimize confinement and plasma compression, and minimizing the diameters of extracted beams. Further, it is shown that this trap will be an excellent device in which to study the physics issues associated with a recently proposed multi-cell trap.

I. Introduction

There are a number of motivations to develop the capability to accumulate large numbers of positrons and create cold, high-density positron plasmas. Applications include positron storage for antihydrogen production [1, 2], electron-positron plasma studies [3], Bose-condensed positronium [4], high resolution measurement of positron scattering and annihilation cross sections with atoms and molecules [5], and the development of portable antimatter traps [6]. The excellent confinement properties of Penning-Malmberg traps make them ideal for the storage of non-neutral plasmas. This paper describes a new 5T trap designed and built to address the physics of cold and high-density positron plasmas. This device is also well suited for studying the issues involved in the accumulation and storage of very large numbers of positrons.

The main factors that inhibit the confinement of high-density single component plasmas are expansion from inherent trap asymmetries and plasma heating from this expansion. A phenomenological model of the background transport combined with limitations from the plasma space charge suggests that the two goals of low temperatures and large total number favor different operating regimes. Consequently, it is of interest to determine the dominant transport mechanisms for high-density non-neutral plasmas ($n \sim 10^{10}$ cm^{-3}) for temperatures ranging from 1 meV to a few eV, a parameter regime that has yet to be fully explored.

CP692, *Non-Neutral Plasma Physics V,* edited by M. Schauer et al.

Cold, low-energy positron beams can be extracted from the trap by decreasing the confinement potential. Cyclotron cooling in large magnetic fields is an effective way to reduce the plasma temperature [7]. Since the energy resolution of a beam formed in this way is determined by the plasma temperature, beams with energy spreads ~ 1 meV should be possible with an electrode structure maintained at 10K. Current positron beams are limited to about 20 meV with room temperature electrodes, so this could improve the achievable energy resolution of these beams by more than an order of magnitude. Also, for plasmas with appreciable space charge, beams with very small diameters ($D \sim 4\lambda_D$) are possible. For example, it is possible to produce a 10μm diameter beam from a positron plasma with $n \sim 10^{10}$ cm^{-3} and $T \sim 10^{-2}$ eV.

To test these ideas, a high-field Penning-Malmberg trap has been constructed. This trap, shown schematically in Fig. 1, uses a warm bore superconducting magnet with a maximum field of 5 tesla, and a two stage pulse-tube cryogenic refrigerator that is designed to cool the electrodes to 10 K inside a 30 K thermal shield. The electrodes (radius R_w=1.27 cm) include two rings that are segmented azimuthally (one 4 sector, and one 8 sector electrode) for the application of rotating electric field perturbations. The density is measured by dumping the plasma out the end onto a phosphor screen and imaged with a CCD camera. For testing purposes, we have installed a thermionic electron gun to fill the trap with electrons.

This paper is organized as follows: In Section II, we describe some fundamental transport issues and basic trap limitations. We combine a simple model of the transport and heating to place limits on the expected operation for various plasma parameters. We also describe measurements of the background transport rate using trapped electrons and compare these measurements to the results of previous experiments on similar traps and to an empirical transport model. Section III describes our initial electron experiments using a rotating electric field to counter the outward transport and produce plasma compression. The observed compression is limited by the outward transport. Data demonstrating a dynamic balance of outward transport and plasma compression is compared to a simple model. Two compression regimes are identified, and differences between the two are highlighted. The technique of extracting small diameter beams is discussed in Section IV. Also discussed is an extension of this technique that could be useful as a diagnostic for the plasma temperature. The design of a multi-cell trap for the storage of more than 10^{12} positrons is discussed in Section V. Concluding remarks are made in Section VI, as well as a discussion of future plans to create specially tailored positron plasmas and beams using the techniques discussed here.

II. Confinement and Cooling

A non-neutral plasma in a Penning-Malmberg trap is confined radially by an axial magnetic field and axially by applied electrostatic potentials. There are several fundamental limits to particle storage in these traps. The Brillouin density limit ($n_B \sim 2\times10^{13}$cm^{-3} for B=5T) [8], is about 100 times greater than the plasma density considered in this paper, so this limit is not a problem. A second limit is the maximum space charge that can be confined by a given potential, V_e, applied to the end electrodes. For a total

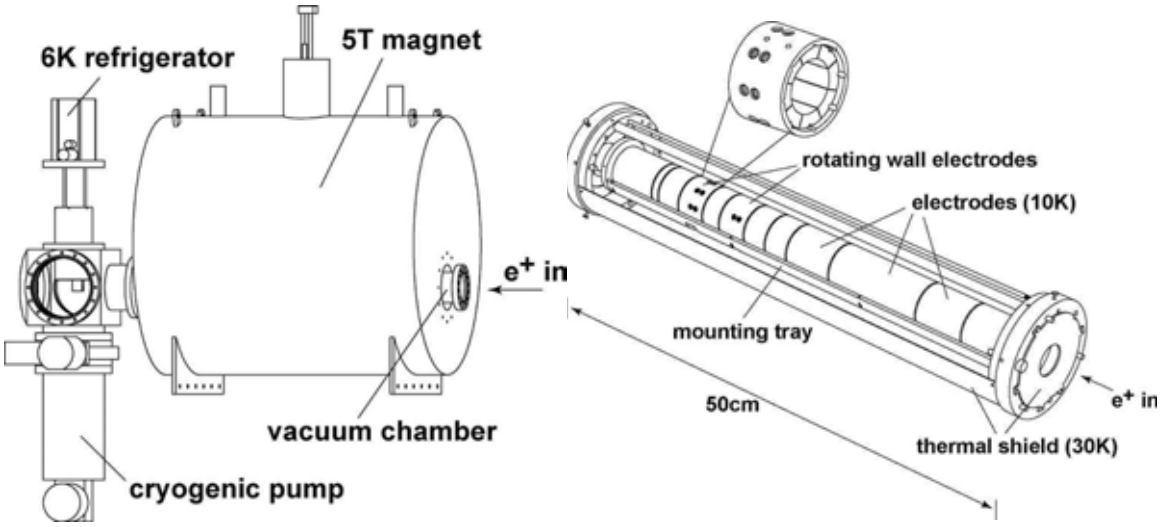

FIGURE 1. Schematic diagram of the high-field trap.

charge $Q_{tot} = eN_{tot}$, plasma length L_p, and radius R_p, in a grounded tube of radius R_w, the space charge potential for a centered rod of positrons is given by:

$$\Phi_{sp} = \frac{eN_{tot}\eta}{L_p}, \qquad (1)$$

where $\eta = 1 + 2\ln(R_w/R_p)$. For example, a plasma with $N_{tot}=10^9$, L=10 cm, $R_p/R_w=0.1$, corresponds to $\Phi_{sp} \sim 80$ V. Thus confining 10^{10} positrons in the same geometry ($\Phi_{sp} \sim 800$ V) would require $V_e \sim 1$ kV on the end electrodes. For the electron plasmas considered in this paper, we use $V_e \leq -100$ V; however, kilovolt potentials will be used in the future to test the physics of the multi-cell trap described in Section V.

The third limit to storing large numbers of positrons is transport from inherent trap asymmetries. For low background gas pressures, the plasma lifetime in Penning-Malmberg traps is limited by small trap asymmetries (eg. electrostatic misalignment of confinement electrodes or inherent magnetic field variations) [9, 10]. The most recent work by Kabantsev et al. demonstrated a strong relationship between the observed transport and the damping of asymmetric trapped particle modes [11, 12]. The detailed link between these modes and particle transport has yet to be elucidated. However, over an extended range of density and temperature, measurements of the plasma transport rate, Γ_O, are observed to be (roughly) characterized by the inverse of the square of the plasma rigidity, i.e. $\Gamma_O \sim R^{-2}$; where $R = f_B/f_R$ is the rigidity, f_B is the axial bounce frequency, and f_R is the ExB rotation frequency [9, 13], as motivated by the theory of bounce-resonant transport [14]. This is observed to be valid in a regime where the plasma is relatively collisionless, and indeed, the R^{-2} dependence is observed to fail in regimes where the plasma is highly collisional [15, 16].

For the purpose of estimating the expected transport rate as a function of plasma parameters, we assume:

$$\Gamma_O = A \times \left(\frac{f_B}{f_R} \right)^{-2} = \frac{\mathrm{A}}{\mathrm{R}^2}, \tag{2}$$

where A is some trap dependent constant. We choose a curve with A=0.016 sec^{-1}, as shown by the solid curve in Fig. 2; this is approximately the best confinement that has been achieved in electron experiments in high B fields (1-5 Tesla), over a broad range of density and temperature [13].

When the plasma expands, it becomes closer to its image charge in the wall resulting in a decrease in electrostatic energy. This decrease in energy results in an increase in the plasma temperature. The heating rate from the background expansion can be written as:

$$\Gamma_{heat} = \left(\frac{1}{\eta} \frac{e\phi_{\mathrm{sp}}}{T_e} \right) \Gamma_O . \tag{3}$$

This formula shows that, for large plasmas, with correspondingly large Φ_{sp}, small background expansion rates are required in order to achieve low plasma temperatures. For the trap described here, this heating is balanced by cyclotron cooling, with a rate given approximately by [7]:

$$\Gamma_{cool} = \frac{1}{4} \left(\frac{\mathrm{B}}{1\mathrm{T}} \right)^2, \tag{4}$$

For B=5T, Eq. 4 gives $\Gamma_{cool} \sim 6.3\ sec^{-1}$.

The plasma transport rate, Γ_O, for electron plasmas in the high-field trap was measured for several different confinement lengths. Typical plasma parameters were $n_0 \sim 2x10^8\ cm^{-3}$, $T_e \sim 300$ K, and $5 < Lp < 30$ cm. These transport measurements are compared with measurements from similar traps in Fig. 2. This transport rate is obtained from the rate of change of the central density, which is approximately exponential with a time constant $\tau = 1/\Gamma_O$. The measured rates are comparable to those predicted by the model, and are close to the best performance observed to date in Penning-Malmberg traps. This gives us confidence in using the model to predict transport rates for trap design purposes, as discussed in Section V.

III. Rotating Wall Experiments

The use of a rotating electric field to counteract inherent trap asymmetries is now common. Electrons [16, 17], ions [18], and positrons [19], have all been successfully confined and compressed using the rotating wall technique. However, a simple model for the compression of the plasma from the applied torque has yet to be developed, particularly in the case of large transport rates. Thus, although it is known experimentally that plasmas can be controlled and compressed, at least to some degree, it

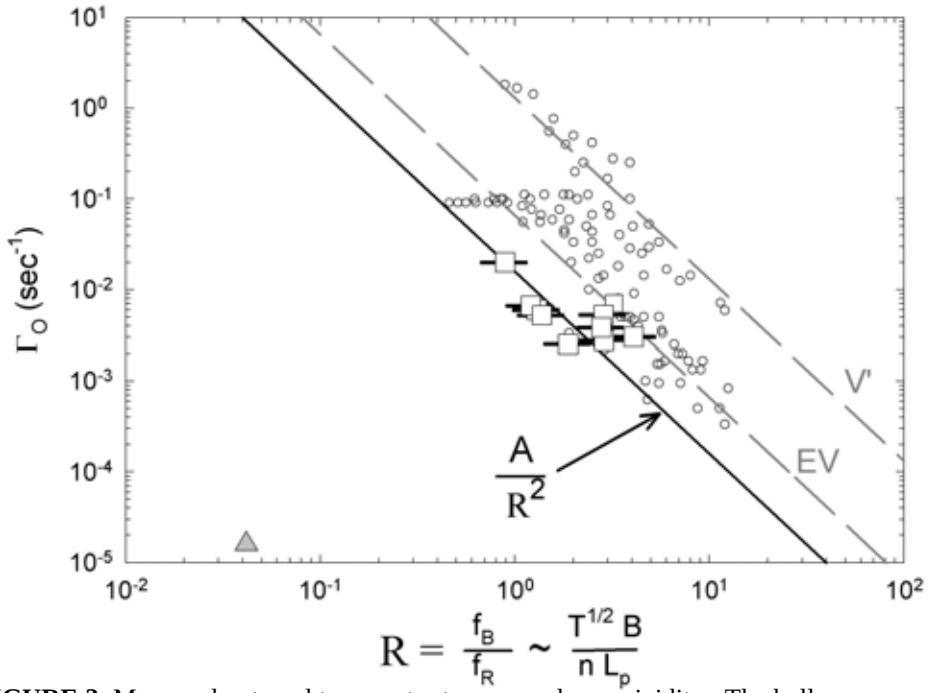

FIGURE 2. Measured outward transport rate versus plasma rigidity. The hollow squares are data from the 5T trap. The hollow circles are data from an older electron trap [14]. The two dashed lines are the older from the V' and EV machines [9]. The solid line corresponds to Eq. 2 with A=0.016 s^{-1}. The triangle is data from Reference [16], and represents the high-collisionality regime.

is currently only through empirical data that the limits of this technique can be determined. A general model has been difficult to develop because the empirical data from different traps and with different mass particles gives different experimental scalings. For example, work with electron plasmas observed only narrow regimes of frequency compression linked to resonances with asymmetric plasma modes. These experiments observed compression rates that scaled linearly with the applied amplitude (i.e. $\Gamma_c \sim V_a^1$) [17]. In contrast, an experiment on positrons, in a different range of plasma parameters, found a broad-frequency non-resonant regime, in which the rate scaled with the square of the applied amplitude (i.e. $\Gamma_c \sim V_a^2$), consistent with the predictions of linear theory [19]. Further, experiments with trapped, laser-cooled ion crystals found a totally different regime in which the plasma rotation phase locked to the frequency of the applied field [20].

Here, we present the results of experiments using a rotating electric field to balance the plasma expansion, including measurement of compression rates for different applied wall amplitudes and drive frequencies. The experimental data indicates two distinct regimes: a broad, non-resonant frequency regime for large drive amplitudes, and a narrow-spectrum, resonant regime at smaller drive amplitudes. Lastly, a simple compression model, utilizing Eq. 2 to describe a dynamic balance between compression and plasma expansion, is compared to experiments in the non-resonant regime.

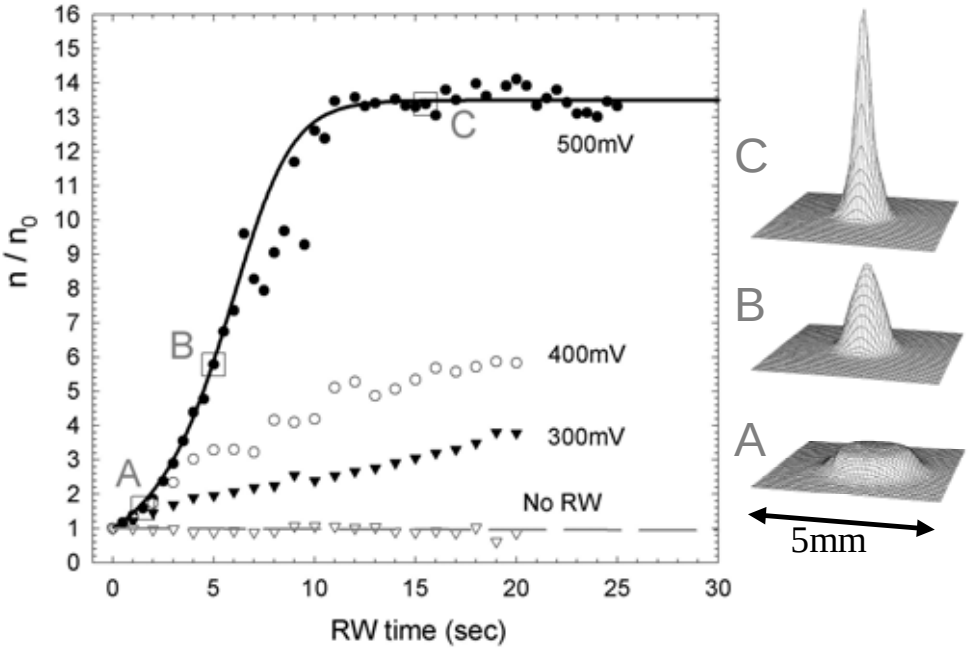

FIGURE 3. Rotating wall compression as a function of time for f_{RW}=8.0 MHz, V_{RW}=300 mV, 400 mV, and 500 mV. For comparison, the decay of the plasma with no applied RW is also shown (dashed line) corresponding to an expansion rate Γ_0=0.0045 s^{-1}. Two-dimensional density profiles are shown on the right, for the points A, B, C labeled on the plot. Fitting to Eq. 6 yields Γ_{in}=0.38 s^{-1}, Γ_0=0.0021 s^{-1}, and peak compression $n_f/n_0=(\Gamma_{in}/\Gamma_0)^{1/2}$=13.5, as shown by the solid curve.

These experiments used a 10 cm long electron plasma confined with the sectored electrode placed near one end, with initial parameters n ~ 5x10^8 cm^{-3}, T ~ 0.1 eV, and R_p ~ 2mm. The applied wave is phased 0°-90°-180°-270° in the same direction as the plasma rotation (i.e. a dipole perturbation with m_θ=1). The plasma is injected and allowed to equilibrate for 1 s. The RF is then turned on at a given applied amplitude (V_{RW}) and frequency (f_{RW}) for a specified amount of time. Then the electrons are accelerated to 6 kV and dumped on a phosphor screen, and the radial profile is measured with a high resolution CCD camera. The compression is measured by taking the ratio of the compressed density n(t) at the center to the initial central density n_0. The compression rate, Γ_c, is given by the ratio of the change in density to the initial density, divided by the compression time, i.e. $\Gamma_c = (n(t)-n_0)/(n_0 \Delta t)$.

Figure 3 plots the compressed plasma density as a function of compression time for an experiment with f_{RW}=8 MHz and V_{RW}=300, 400, and 500 mV. For comparison the density evolution with no applied RW field is also shown. For the lower amplitudes, we observe a continual rise in the density with time. However, for V_{RW}=500 mV, over the same time period, a quick rise in central density is observed which then plateaus at a compression factor of ~13.

A simple extension of the transport model from Section II can be used to predict the plasma evolution under some very restrictive assumptions. Assuming that the inward

compression rate (Γ_{in}) is independent of time, density, and temperature, and utilizing the empirical outward transport rate dependence on density ($\Gamma_O \propto n^2$), we can write an evolution equation for the plasma density of the form:

$$\frac{1}{n}\frac{dn}{dt} = \Gamma_{in} - \Gamma_O = \Gamma_{in} - \Gamma_0\left(\frac{n}{n_0}\right)^2. \quad (5)$$

This has the analytic solution:

$$\frac{n(t)}{n_0} = \sqrt{\frac{\Gamma_{in}/\Gamma_0}{1+(\Gamma_{in}/\Gamma_0 - 1)e^{(-2\Gamma_{in}t)}}}. \quad (6)$$

When this model for the time evolution of the density is fit to the data in Fig. 3, we find Γ_{in} = 0.38 s^{-1}, Γ_0 = 0.0021 s^{-1} (solid line), with a steady-state compression ratio of n_f/n_0=13.5. It is interesting to note that the fit to Γ_0 is within a factor of two of the independently measured outward rate of Γ_O = 0.0045 s^{-1}. This agreement is somewhat surprising since we neglected the evolution of the plasma temperature. This may be due to the fact that the cyclotron cooling rate is rapid compared to the other time scales in the problem.

A similar equation for the plasma temperature can be written using Eqs. 3 and 4. This could then be solved self consistently with the assumed temperature dependence of the outward transport rate. These coupled equations can be solved numerically to obtain a more refined comparison with the experimental measurements. A more complete test of the model will require measuring the time dependence of the plasma temperature, which we plan to do.

Figure 4 shows the compression rate as a function of applied amplitude for three different applied frequencies. Over a broad range in amplitude, the compression rates scale like $\Gamma_C \propto V_{RW}^2$. This is similar to the scaling observed previously for warm positron plasmas [19].

Figure 5 shows the measured compression rate as a function of applied frequency for three different applied amplitudes. Over a broad range in frequency, the compression rates scale closely to $\Gamma_C \propto f_{RW}^2$. At present, we have no explanation for this scaling. However, since we have no data on the heating associated with the compression, this frequency scaling could be an indication of higher plasma temperatures caused by an increase in heating at higher frequencies. The model suggests that as the temperature increases, the background transport rate decreases. Thus, for a given input torque (fixed drive amplitude), we would observe a higher compression rate at higher temperatures, which is qualitatively consistent with the data. These scalings must be compared to an experimentally measured plasma temperature before definite conclusions can be made.

All of the data presented thus far have been at relatively high drive amplitudes (V > 200mV). Frequency scans were also performed at low amplitudes (e.g. 50mV and 100mV) and are shown in Fig. 6. In this regime, we do not observe a broad frequency dependence to the compression rate, but rather the compression is now sharply peaked at several discrete frequencies. These frequencies are close to the calculated Trivelpiece-

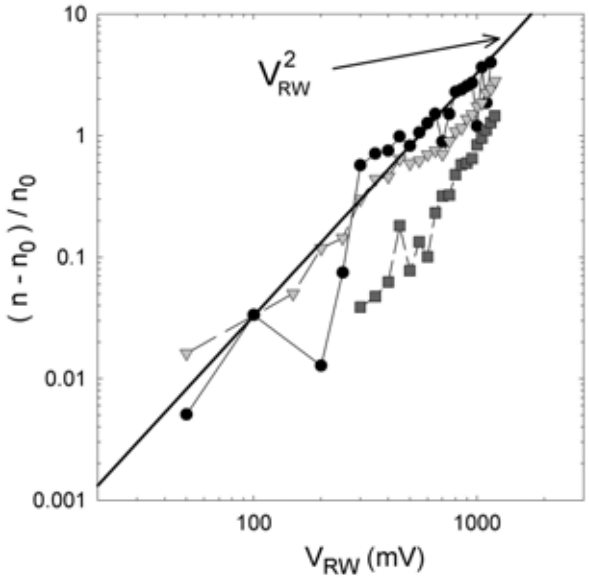

FIGURE 4. Rotating wall compression rate (after 2 s) as a function of applied drive amplitude for three different frequencies. Circles, triangles, squares are 8 MHz, 6 MHz, 4 MHz, respectively. The solid line is $\Gamma_C \propto V_{RW}^2$.

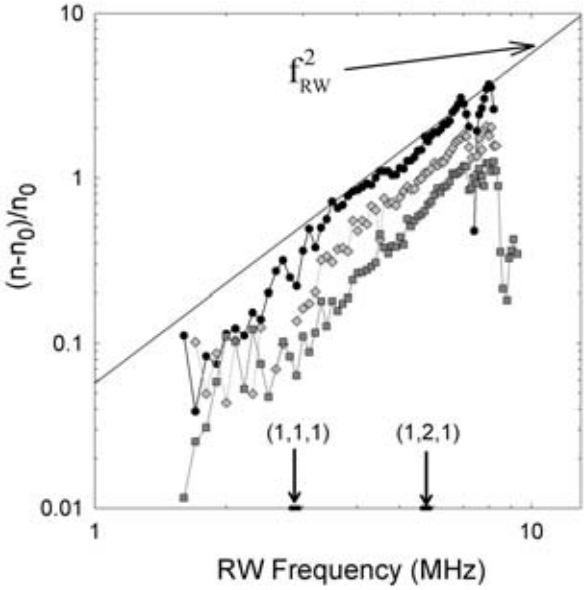

FIGURE 5. Rotating wall compression rate (after 2 s) as a function of applied frequency for three different applied amplitudes. The circles, diamonds, squares, are 1.0 V, 0.8 V, 0.6 V, respectively. The lowest calculated TG mode frequencies (m_θ, m_z, m_r) are shown by the arrows. The solid line is $\Gamma_C \propto f_{RW}^2$.

FIGURE 6. Plasma compression after 30 s versus frequency for low amplitude drive. The solid circles are V_{RW}=50 mV, the grey triangles are V_{RW}=100 mV. The calculated values of the lowest Trivelpiece-Gould modes (m_θ, m_z, m_r) are shown by the arrows.

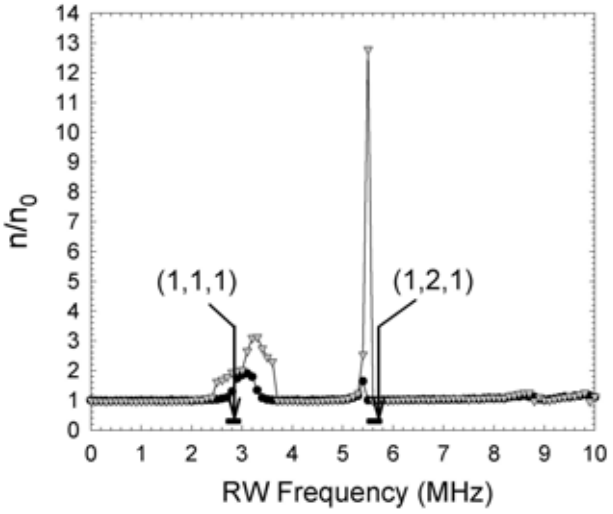

Gould mode frequencies, as indicated by the arrows [21]. This resonant regime is similar to that observed previously in electron plasmas [17]. The exact crossover between the two different regimes has yet to be identified, but it appears that there is a relatively distinct transition between the two.

A closer look at the compressed profiles shows a qualitative difference between the two regimes. Figure 7(a) shows the initial flat-top profile before compression. Figure 7(b), shows the steady-state profile after 15 s with a large drive amplitude (500 mV).

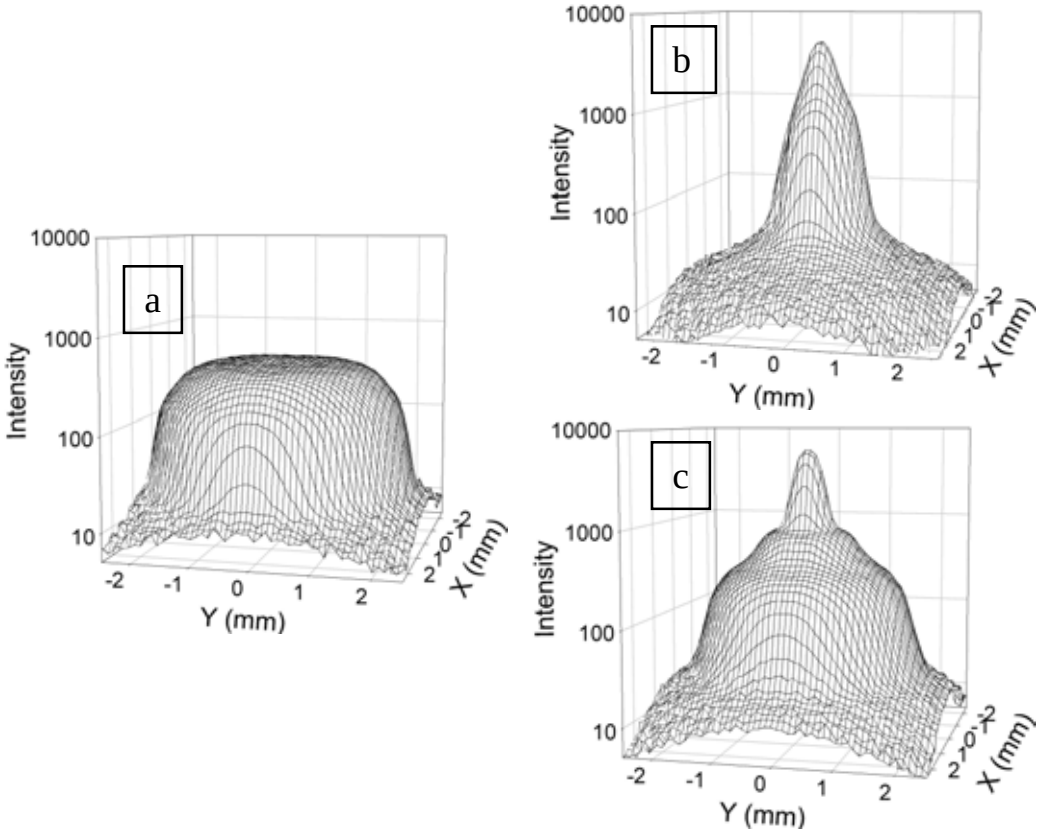

FIGURE 7. Comparison of steady-state profiles for non-resonant compression and resonant compression of an initial flat-top plasma: (a) initial plasma. (b) after 15 s with f_{RW} = 8 MHz and V_{RW} = 500 mV. (c) after 30 s of resonant compression with f_{RW} = 5.5 MHz and V_{RW} = 100 mV.

Profile 7(b) is peaked with a low level, diffuse background just above the noise floor. Figure 7(c) shows an example of one of the resonant peaks (5.5 MHz) at low drive amplitude (100 mV). This profile has a narrow peak at the center and a rather broad halo that has a much higher density as compared with the large-amplitude case. These different profiles are likely indications that different mechanisms are responsible for the compression in the two regimes. For example, the low amplitude case could reflect coupling to weakly damped TG modes [17], whereas the large amplitude case could be due to particle bounce-resonance coupling [22].

IV. Extraction of Small Diameter Beams

If the end confinement electrode is slowly lowered to a potential close to the plasma space charge potential, particles with the highest energy (i.e. the high energy tail of the Maxwellian velocity distribution) are able to leave the trap. Since the confinement potential provided by the electrodes is a minimum on the trap axis, the first particles

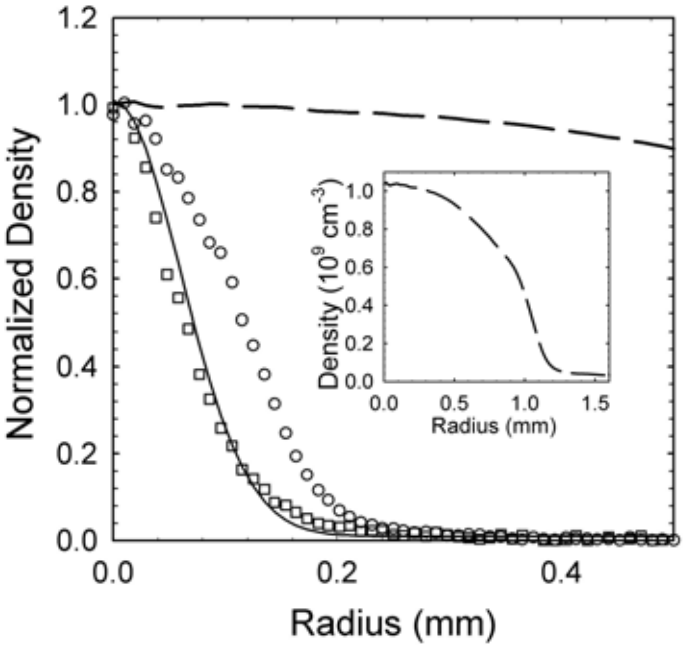

FIGURE 8. Radial profile of small beams ejected from a broad, dense electron plasma. The dashed curve is the initial plasma. The hollow circles and squares are for two different levels of ejection, n_b/n_0=0.51 and n_b/n_0=0.32 respectively. The solid curve is a fit of Eq. 7 to the hollow squares, with a beam radius of ~ 60 μm. The inset is an expanded view of the initial plasma profile.

exiting the trap will be near the plasma center. For small particle loss (i.e. $\Delta n_0 < n_0/2$), the radial profile of the ejected plasma will be approximately Gaussian, with a beam density, $n_b(r)$, of the form [23]:

$$n_b(r) = C n_0(r) \exp\left(-\left(\frac{r}{2\lambda_D}\right)^2\right), \qquad (7)$$

where λ_D is the plasma Debye length and the constant C depends on the ratio of the electrode potential to the plasma space charge potential. For plasmas with $R_p >> \lambda_D$, the ejected beam will have a diameter, $D \sim 4\,\lambda_D$ (which for cold, T~1 meV, and dense, $n \sim 10^{10}$ cm^{-3}, plasmas can be less than 10 μm).

The radial profiles of two ejected beams are shown in Fig. 8 along with the profile of the initial plasma. For this case, the central plasma density is 1.2×10^9 cm^{-3}; assuming the plasma is at a temperature T ~ 300 K (i.e. 25 meV), we estimate a Debye length of 34 μm. Fitting a Gaussian to the smallest beam, gives a measured half-width of 60 μm. From Eq. 7, the beam half-width is $2\lambda_D \sim 68$ μm, which is within about 10% of measured beam radius.

Measurement of the profile of an ejected beam can also be used to estimate the plasma Debye length, λ_D. Thus, if the density profile is known, an estimate of the plasma temperature can be made. This technique is limited by the assumption of uniform

plasma temperature as a function of radius, and that the particle ejection is fast compared to the transport and equilibration times, but slow compared to the particle bounce frequency, f_b, and any plasma mode frequency. Further, only the initial pulse from the unperturbed plasma can be used. After such a pulse, the plasma will be slightly hollow, and instabilities can develop which would alter the ejected plasma profile.

V. Multi-cell Trap

Recently a novel, multi-cell Penning-Malmberg trap has been proposed that is designed to confine more than 10^{12} positrons in plasmas with lifetimes of days or longer [24]. A 10 tesla magnetic field and 10 kV electrode potentials are assumed to confine the plasma in a cryogenically cooled electrode structure (T~10 K). One set of constraints on the operating parameters arises from the previously described outward, asymmetry-driven transport and the associated expansion heating. The transport rate was assumed to be given by the empirical transport scaling from Sect. II (Eq. 2). This inherent expansion will be balanced by radial compression from a rotating electric field. It was also assumed that the heating associated with this transport will be balanced by cyclotron cooling in the 10 T field ($\Gamma_{cool} \sim 25\ s^{-1}$). End potentials of $V_e = 10$ kV, provide the capability to confine plasmas up to a maximum plasma space charge potential of 10 kV. The transport and cooling considerations favor high plasma temperatures; for positrons, this is limited by positronium atom formation on the residual background gas ($p \sim 10^{-12}$ torr). These considerations lead to a multi-cell design in which separate plasmas are confined in cylindrical electrodes ~ 1 cm in diameter and 1 cm in extent along the magnetic field. Typical plasma parameters are proposed to be $T_e \sim 2$ eV, $n \sim 10^{11}\ cm^{-3}$ and a plasma radius ~ 1.5 mm. A trap for 10^{13} positrons could be confined in 10^3 cells housed in an electrode structure 15 cm in diameter and 30 cm long (immersed in the common 10 T field).

Although the proposed trap is ambitious, the basic physics issues involved with the operation of such a trap can be investigated using the high field trap described here. A 1 kV confining potential and 5 T magnetic field, will allow for the confinement of 10^{10} positrons, with L_p=10 cm, R_p=1 mm, R_w=1.27 cm, and $n \sim 3 \times 10^{10}\ cm^{-3}$. Assuming a plasma temperature of 2 eV, Eq. 2 predicts an outward rate of $\Gamma_O \sim 0.033\ s^{-1}$, and Eq. 3 predicts a heating rate of $\Gamma_{heat} \sim 2.7\ s^{-1}$, which is less than the cyclotron cooling rate at 5T of $\Gamma_{cool} \sim 6.3\ s^{-1}$. Further, the trap will accommodate an electrode stack with up to 10 radial cells, and 10 axial cells. Assuming 10^{10} positrons per cell, this would give a total of 10^{12} stored positrons. Such a device could form the basis for a portable positron trap. For example, a 25 mCi ^{22}Na source and neon moderator can produce about 10^6 moderated positrons per second. For a trap with 10^{12} stored positrons, this is equivalent to 10^6 seconds, or about 11 days of continuous operation.

Several challenges need to be addressed before this can be accomplished. First, the transport physics of high-density non-neutral plasmas ($n \sim 10^{10}\ cm^{-3}$) needs to be characterized. Further, a robust model of plasma confinement using a rotating electric field needs to be validated and verified in the high-density regime. A technique for the stacking and manipulation of large numbers of positrons, specifically into different radial cells, needs to be developed, as well as an efficient method of extraction from these cells.

These challenges can be addressed with a small number of cells in the current high-field trap.

An additional challenge is operating with a suitable positron source. The current buffer gas trap can provide about 500 million positrons every 5 minutes. Consequently, it would take about 7 days of continuous operation to fill to 10^{12} positrons. Thus, to obtain the full potential of the multi-cell trap described here (e.g. $N_{e+} > 10^{12}$), will require either a reactor-based or LINAC positron source or a stronger radioactive source (e.g. ≥ 1 Ci ^{22}Na).

VI. Concluding Remarks

We report first results using a specially designed high-field, cryogenic Penning-Malmberg trap that is designed to confine large numbers of positrons and produce cold plasmas and beams. Electron plasmas were used to determine the optimum operating regime with the electrode structure at 300 K. The experiments indicate that a simple model of rotating wall compression, balancing expansion heating and cyclotron cooling, qualitatively describes the plasma compression and resulting dynamic steady state. Density compression factors ≥ 10 were obtained, resulting in plasma densities ≥ $5x10^9$ cm^{-3}. First attempts to extract small-diameter beams from the plasma center were successful with beam diameters, D, approaching the expected theoretical limit $D \sim 4\lambda_D$.

Experiments with positrons are planned for the near future. Bursts of positrons ($N \sim 5 \times 10^8$) will be transferred from the existing buffer-gas trap to the high-field trap on a 5 minute cycle. The positrons will be transferred through a pulsed valve to minimize contamination of the cryogenic, UHV trap. Based upon previous experience [1] and using a set of specially designed electrodes in the region of rapidly varying magnetic field, transfer efficiencies ≥ 70% are expected. Positron plasmas with $N \sim 10^{10}$ can be accumulated in ~ 2 hours. The trap described here is also expected to be well suited to testing the design of a multicell Penning-Malmberg trap capable of confining orders of magnitude more positrons, since the optimum parameters of the multicell trap are not far from the operating range of the present device.

VII. Acknowledgements

This work was supported by the Office of Naval Research, grant #N00014-02-1-0123. The authors acknowledge the expert technical assistance of E. A. Jerzewski and R.G. Greaves for helpful conversations and collaboration on the multi-cell trap.

Finally, we take this opportunity to acknowledge the long-term support of ONR. The positron plasma research that led to the development of the efficient buffer-gas trap [25-27], solid neon positron moderator [28], cold positron beam [29], rotating wall compression of positron plasmas [19, 30], a wide variety of plasma and atomic physics results [30-33], and the high-field cryogenic trap described here would not have been possible without the ONR support and the support and encouragement of ONR program officer C. W. Roberson.

References:

1. Amoretti, M., Amsler, C., Bonomi, G., *et al*., *Nature* **419**, 456 (2002).
2. Gabrielse, G., Bowden, N., Oxley, P., *et al*., *Phys. Rev. Lett.* **89**, 213401 (2002).
3. Greaves, R. G. and Surko, C. M., *Non-Neutral Plasma Physics IV, edited by F. Anderegg, et al. (American Institute of Physics)* , 10-23 (2002).
4. Mills, A. P., Jr., *Nucl. Instrum. and Meth.* **192**, 107-116 (2002).
5. Sullivan, J. P., Gilbert, S. J., Marler, J. P., *et al*., *Phys. Rev. A* **66**, 042708-1-12 (2002).
6. Greaves, R. G., Gilbert, S. J., and Surko, C. M., *Appl. Surf. Sci.* **194**, 56 (2002).
7. O'Neil, T., *Phys. of Fluids* **23**, 725 (1980).
8. Davidson, R. C., *"Physics of Nonneutral Plasmas" (Addison-Wesley, Reading, MA, 1990)* .
9. Driscoll, C. F. and Malmberg, J. H., *Physical Review Letters* **50**, 167-70 (1983).
10. Kriesel, J. M. and Driscoll, C. F., *Phys. Rev. Lett.* **85**, 2510 (2000).
11. Kabantsev, A. A. and Driscoll, C. F., *Phys. Rev. Lett.* **89**, 245001 (2002).
12. Hilsabeck, T. J., Kabantsev, A. A., Driscoll, C. F., *et al*., *Phys. Rev. Lett.* **90**, 245002 (2003).
13. Cluggish, B. P., *University of California, San Diego Thesis* (1995).
14. Eggleston, D. L. and O'Neil, T., *Phys. of Plasmas* **6**, 2699 (1999).
15. Malmberg, J., O'Neil, T. M., Hyatt, A. W., *et al*., *Proc. of the Sendai Symposium on Plasma Nonlinear Electron Phenomena* , 31-35 (1984).
16. Hollmann, E. M., Anderegg, F., and Driscoll, C. F., *Phys. of Plasmas* **7**, 2776-89 (2000).
17. Anderegg, F., Hollmann, E. M., and Driscoll, C. F., *Phys. Rev. Lett.* **81**, 4875-4878 (1998).
18. Huang, X. P., Anderegg, F., Hollmann, E. M., *et al*., *Phys. Rev. Lett.* **78**, 875 (1997).
19. Greaves, R. G. and Surko, C. M., *Phys. Rev. Lett.* **85**, 1883-1886 (2000).
20. Huang, X. P., Bollinger, J. J., Mitchel, T. B., *et al*., *Phys. Rev. Lett.* **80**, 730 (1998).
21. Trivelpiece, A. W. and Gould, R. W., *J. of Appl. Phys.* **30**, 1784-1793 (1959).
22. Crooks, S. M., *University of California, San Diego Thesis* (1995).
23. Eggleston, D. L., Driscoll, C. F., and Beck, B. R., *Physics of Fluids B* **4**, 3432-9 (1992).
24. Surko, C. M. and Greaves, R., *J. Rad. Chem.* **in press** (2003).
25. Murphy, T. J. and Surko, C. M., *Phys. Rev. A* **46**, 5696-705 (1992).
26. Greaves, R. G. and Surko, C. M., *Non-Neutral Plasma Phys. III, edited by John J. Bollinger, et al., (American Institute of Physics, Princeton, NJ)* **498**, 19-28 (1999).
27. Greaves, R. G. and Surko, C. M., *Canadian Journal of Physics* **51**, 445-8 (1996).
28. Gilbert, S. J., Kurz, C., Greaves, R. G., *et al*., *Appl. Phys. Lett.* **70**, 1944-1946 (1997).
29. Greaves, R. G. and Surko, C. M., *Phys. Plasmas* **8**, 1879-1885 (2001).
30. Greaves, R. G. and Surko, C. M., *Phys. Plasmas* **4**, 1528-1543 (1997).
31. Gilbert, S. J., Dubin, D. H. E., Greaves, R. G., *et al*., *Phys. Plasmas* **8**, 4982-94 (2001).
32. Iwata, K., Greaves, R. G., Murphy, T. J., *et al*., *Phys. Rev. A* **51**, 473 (1995).
33. Barnes, L. D., Gilbert, S. J., and Surko, C. M., *Phys. Rev. A* **67**, 032706 (2003).